A stable mesh-independent approach for numerical modelling of structured soils at large strains

Lluís Monforte[a,*], Matteo O. Ciantia[b], Josep Maria Carbonell[c], Marcos Arroyo[a], Antonio Gens[a]

[a]*Department of Civil and Environmental Engineering, Universitat Politècnica de Catalunya - BarcelonaTech, Spain*
[b]*University of Dundee, Dundee, United Kingdom*
[c]*International Center for Numerical Methods in Engineering (CIMNE), Barcelona, Spain*

Abstract

We describe the large strain implementation of an elasto-plastic model for structured soils into G-PFEM, a code developed for geotechnical simulations using the Particle Finite Element Method. The constitutive model is appropriate for naturally structured clays, cement-improved soils and soft rocks. Structure may result in brittle behavior even in contractive paths; as a result, localized failure modes are expected in most applications. To avoid the pathological mesh-dependence that may accompany strain localization, a nonlocal reformulation of the model is employed. The resulting constitutive model is incorporated into a numerical code by means of a local explicit stress integration technique. To ensure computability this is hosted within a more general Implicit-Explicit integration scheme (IMPLEX). The good performance of these techniques is illustrated by means of element tests and boundary value problems.

Keywords: PFEM, structured soils, nonlocal elasto-plasticity, constitutive modeling

1. Introduction

Inspired by a large body of experimental evidence (Leroueil and Vaughan, 1990) several elasto-plastic constitutive models incorporating structure have been proposed (Gens and Nova, 1993; Rouainia and Muir Wood, 2000; Liu and Carter, 2002). These models can represent the behavior of soft rocks (e.g. Lagioia and Nova, 1995; Ciantia and di Prisco, 2016; Ciantia et al., 2018), natural clays (e.g. Wheeler et al., 2003) or artificially cemented soils (e.g. Rios et al., 2016). Structure enhances the brittleness of response along compression-dominated paths. Adding this realistic feature to constitutive descriptions is beneficial for more accurate predictions of structural response (Taiebat et al., 2010; Gonzalez et al., 2012; Arroyo et al., 2012; Yapage et al., 2014). Because of the relative complexity of these models numerical solution is required for practical applications. Unfortunately, the simulation of brittle material responses is conductive to strain localization.

Strain localization poses two numerical challenges - mesh dependency of the solution and computability of the solution (Oliver et al., 2008)- that need to be addressed to develop reliable numerical algorithms. In the context of Finite Elements, strain localization tends to take place along single element-wide zones and the direction of the shear band is typically controlled by the preferential alignment of the elements (Zienkiewicz et al., 1995; Galavi and Schweiger, 2010). A numerical size effect also appears since, as the mesh is refined, the thickness of the shear band decreases and the energy dissipated in the shear band tends to zero. As a consequence, the load-displacement curves and structural responses are also mesh-dependent.

This pathological mesh-dependence is not exclusive of elasto-plastic problems, appearing also in other constitutive models that exhibit brittle or quasi-brittle behavior, e.g. damage models (de Pouplana and Oñate, 2016; Jin and Arson, 2018a). This has increased the interest on regularization techniques and several, applicable across different constitutive models, have been developed. These regularization techniques incorporate a length scale to the constitutive law, which mitigates the mesh-dependency of the problem by enforcing the width of the localized region.

Within regularization techniques, the nonlocal integral type solution has the advantage of not changing the field equations which facilitates numerical implementation (Bažant and Jirásek, 2002; Lu et al., 2009; Galavi and Schweiger, 2010; Jin and Arson, 2018a,b; de Pouplana and Oñate, 2016; Summersgill et al., 2017a; Goodarzi and Rouainia, 2017; Mánica et al., 2018). In this approach chosen nonlocal variables are valuated from spatially averages of field variables in a neighborhood, and the constitutive models is updated by replacing a local variable with its nonlocal counterpart. Consequently, the constitutive response of a Gauss point is influenced by all the integration points within a neighborhood, which size is determined with a characteristic length.

Strain localization may also pose another numerical difficulty when an implicit time-marching scheme is used for the global problem: the numerical convergence rate may be seriously affected. In cases where strain softening appears in the constitutive model, the global system of non-linear equations becomes highly sensitive to small changes. The stiff-

*Corresponding author

ness matrix of the Newton-Raphson method may become so ill-conditioned that no convergence might be achieved even if using very small time-steps (Alfano and Crisfield, 2001; Lorentz and Badel, 2004; Oliver et al., 2008; Lu et al., 2009). Alternative ways to solve the nonlinear system of equations, namely arc-length methods (Riks, 1979), are not always reliable and may also fail to achieve convergence (Hellweg and Crisfield, 1998; Alfano and Crisfield, 2001).

To address these issues, Oliver et al. (2008) proposed a numerical technique, the so-called IMPLEX, for the integration of constitutive models that provides enhanced robustness and computability with respect to usual methods. This scheme, or variations of it, has been successfully applied to thermo-mechanical problems (Rodríguez et al., 2016, 2017), single-phase geomechanical problems with simple elasto-plastic constitutive responses (Prazeres et al., 2016) and even the integration of gradient-enhanced damage models (Titscher et al., 2019).

Little attention seems to have been paid to the numerical problems associated with strain localization in structure-enhanced elasto-plastic models or to their generalization for large strain problems. This may be related to an initial application focus on the pre-failure small-strain range. However, robust and accurate algorithms able to deal with the post-peak range are necessary for a broad range of engineering applications. For instance, models at large strains are necessary to simulate in situ test like the CPTu (Gens et al., 2016; Monforte et al., 2018) or to understand the complex behavior of piles installed in chalk (Jardine et al., 2018).

This work aims to fill that gap, describing the procedures followed to achieve a stable mesh-independent implementation of an elasto-plastic structure-enhanced constitutive model into a numerical finite element code for simulation of boundary value problems involving large strains. In what follows the constitutive framework employed is first described, including the algorithm applied for large strain stress-point integration. Then we describe how, to alleviate mesh dependency, that algorithm was modified to incorporate nonlocal effects. We then introduce the specific IMPLEX stress integration scheme developed to ensure computability in boundary value problems. The accuracy and robustness of the numerical schemes are first illustrated in a number of elementary-level laboratory tests. Finally, a set of representative simulations, namely biaxial tests and the indentation of a rigid footing into a poromechanical medium, are presented to showcase the reliability of the numerical approach.

2. Constitutive equations

In this section first the constitutive framework in which the model is formulated -large strain elasto-plasticity (Simo and Hughes, 1998)- is briefly described. Afterwards, the constitutive model for structured clays will be presented.

2.1. Constitutive framework at large strain

Objective stress transformation and frame invariance are key requirements for any large strain constitutive framework, necessary to avoid spurious stress variations under rigid body motions. Two different such frameworks are currently in use for the formulation of large deformation elasto-plasticity (Simo, 1998; Simo and Hughes, 1998).

The first one is based on the use of hypoelastic rate models and an additive decomposition of the spatial rate of deformation tensor into an elastic and plastic part. These kind of schemes are regarded as extension of usual small strains algorithms to the large strain regime, since additional terms are added in order to deal with the rigid body rotation and ensure the objectivity of the resulting stress increment. Because of this, it is believed that the use of such formulation is more appropriate for problems involving large displacements and rotations but small strains (Bathe, 2006).

In the second approach, deformation itself (and not a rate) is decomposed multiplicatively into an elastic and plastic part (Simo and Hughes, 1998). This approach is best suited to problems involving large displacements and large deformations and is the one adopted in this work.

The main difference with the small strain theory is the replacement of the additive decomposition of the infinitesimal strain field by a multiplicative decomposition of the deformation gradient into elastic and plastic parts. To do so an intermediate configuration of irreversible (plastic) deformations is introduced, relative to which the elastic response of the material is characterized. Using the chain rule the deformation gradient, $\mathbf{F}$, is defined as:

$$\mathbf{F} = \frac{\partial \boldsymbol{\phi}(\mathbf{X}, t)}{\partial \mathbf{X}} = \mathbf{F}^e \cdot \mathbf{F}^p \tag{1}$$

where $\boldsymbol{\phi}(\mathbf{X}, t)$ is the motion of the continuum body whereas $\mathbf{F}^e$ and $\mathbf{F}^p$ are, respectively, the elastic and plastic deformation gradients.

For ease of reference, the main governing equations for non-associative plasticity within this framework are summarized in Table 1(first column) (Simo and Meschke, 1993; Simo, 1998). It is assumed that both the hyper-elastic and plastic responses are isotropic; the hyperelastic model is formulated in terms of the Hencky strain. There are a set of internal variables (strain-like), β, whose temporal derivative is a function of the plastic velocity gradient, $\mathbf{l}^p$; stress-like internal variables (z) may be explicitly computed from the evolution of the strain-like ones.

2.2. Constitutive model for structured soils

The constitutive model for structured clayey materials proposed in this work is built around the Modified Cam Clay model. Therefore, the yield surface is defined simply as:

$$f(\boldsymbol{\tau}, p_s, p_t) = \left(\frac{q}{M}\right)^2 + p^\star \left(p^\star - p_c^\star\right) \tag{2}$$

where $q = \sqrt{3\, J_2}$ and J_2 is the second invariant of the Kirchhoff stress tensor $\boldsymbol{\tau}$. M is the slope of the Critical state line in the $p' - q$ plane and

$$p^\star = p' + p_t \tag{3}$$

$$p_c^\star = p_t + p_s + p_m \tag{4}$$

Table 1: Basic relations of the elasto-plastic local and nonlocal models. If not redefined, the nonlocal model inherits the expression of the local model.

	Local model	Nonlocal model
Strain decomposition:	$\mathbf{F} = \mathbf{F}^e \cdot \mathbf{F}^p$	
Hyperelastic model:	$\boldsymbol{\tau} = \dfrac{\partial w(\boldsymbol{\epsilon}^e)}{\partial \boldsymbol{\epsilon}^e}$ where $\boldsymbol{\epsilon}^e = \dfrac{\ln\left(\mathbf{F}^e \cdot \mathbf{F}^{e\,T}\right)}{2}$	
Yield surface:	$f(\boldsymbol{\tau}, z) \leq 0$	$f(\boldsymbol{\tau}, \tilde{z}) \leq 0$
Flow rule:	$\mathbf{l}^p = \dot{\gamma}\dfrac{\partial G(\boldsymbol{\tau}, z)}{\partial \boldsymbol{\tau}}$	$\mathbf{l}^p = \dot{\gamma}\dfrac{\partial G(\boldsymbol{\tau}, \tilde{z})}{\partial \boldsymbol{\tau}}$
Hardening law:	$\dot{\beta} = h(\mathbf{l}^p) \qquad z = z(\beta)$	$\dot{\beta} = h(\mathbf{l}^p) \qquad \tilde{z} = z(\tilde{\beta})$
Nonlocal relation:		$\tilde{\beta} = \dfrac{\int_\Omega w\,\beta\,\mathrm{d}\Omega}{\int_\Omega w\,\mathrm{d}\Omega}$
Kuhn-Tucker conditions:	$\dot{\gamma} \geq 0 \qquad f \leq 0 \qquad \dot{\gamma} f = 0$	
Consistency condition	$\dot{\gamma}\dot{f} = 0$	

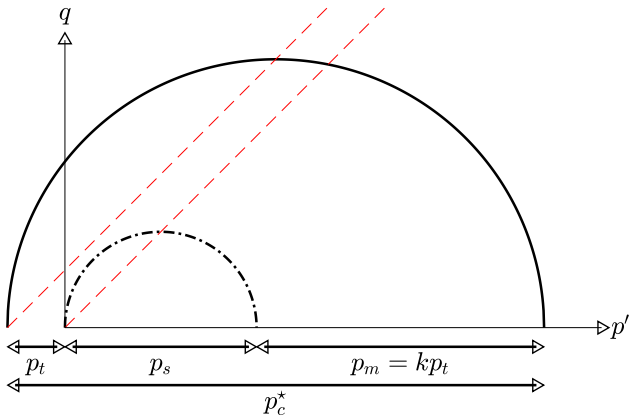

Figure 1: Yield surface in the $p - q$ plane for axisymmetric compression.

where $p' = \mathrm{tr}(\boldsymbol{\tau})/3$ is the first invariant of the Kirchhoff stress tensor.

The shape of the yield locus in the triaxial plane and the plastic variables p_s, p_t, p_m and $p_c^\star$ are graphically illustrated in Figure 1. The variable p_s acts as the preconsolidation stress of the unstructured soil. In contrast, p_t and p_m account for the effects of structure implying: (i) a non-zero tensile strength ($p_t > 0$) (Gens and Nova, 1993; Ciantia et al., 2015) and (ii) an increase in the yield stress along radial loading paths, thus, p_m corresponds to such an increase in case of an isotropic compression path.

The quantities p_m and p_t can be considered as two independent hardening variables; however, they are usually assumed to be related to each other by the simple proportional rule (Ciantia and di Prisco, 2016):

$$p_t = k\, p_m \tag{5}$$

The hardening variables evolve in terms of the volumetric and distortional plastic flow (Tamagnini and Ciantia, 2015, 2016):

$$\dot{p}_s = \rho_s\, p_s \left(\mathrm{tr}\,(\mathbf{l}^p) + \chi_s \sqrt{\frac{2}{3}}\, \|\mathrm{dev}\,(\mathbf{l}^p)\,\| \right) \tag{6}$$

$$\dot{p}_t = \rho_t\, p_t \left(|\mathrm{tr}\,(\mathbf{l}^p)\,| + \chi_t \sqrt{\frac{2}{3}}\, \|\mathrm{dev}\,(\mathbf{l}^p)\,\| \right) \tag{7}$$

where ρ_t, χ_t, ρ_s, and χ_s are constitutive parameters and $\mathbf{l}^p$ is the spatial plastic velocity gradient, which may be also described as (Simo, 1998):

$$\mathbf{l}^p = \mathbf{F}^e \cdot \dot{\mathbf{F}}^p \cdot \mathbf{F}^{-1} = \mathbf{l} - \mathbf{l}^e \tag{8}$$

where $\mathbf{l} = \nabla \mathbf{v}(\mathbf{x}, t)$ and $\mathbf{l}^e$ are, respectively, the total and elastic velocity gradients whereas $\mathbf{v}(\mathbf{x}, t)$ stands for the velocity of the deformable body.

It is of interest for the later formulation of nonlocal effects to obtain an explicit expression in terms of the plastic internal variables of p_s and p_t by integrating in time Equations (6) and (7). Note first that the trace of the plastic velocity gradient coincides with the temporal derivative of the plastic Hencky volumetric strain, hence,

$$\dot{\epsilon}_v^p = \mathrm{tr}(\mathbf{l}^p) \tag{9}$$

and let us define,

$$\dot{\alpha} = \|\mathrm{dev}\,(\mathbf{l}^p)\,\| \qquad \bar{\epsilon}_v^p = \int_0^t |\mathrm{tr}(\mathbf{l}^p)|\,\mathrm{d}t \tag{10}$$

Then, the stress-like hardening parameters -Equations (6) and (7)- might be explicitly computed from the plastic internal

variables ϵ_v^p, $\bar{\epsilon}_v^p$ and α as:

$$p_s = p_{s_0} \exp\left(\rho_s \left(\epsilon_v^p + \chi_s \sqrt{\frac{2}{3}}\,\alpha\right)\right) \tag{11}$$

$$p_t = p_{t_0} \exp\left(\rho_t \left(\bar{\epsilon}_v^p + \chi_t \sqrt{\frac{2}{3}}\,\alpha\right)\right) \tag{12}$$

The elastic response is characterized by means of an hyperelastic model incorporating a tensile range (Houlsby, 1985; Tamagnini et al., 2002), which in this work it is formulated in terms of the Hencky strain and the Kirchhoff stress tensor. Finally, please note that the current formulation has been developed to include non-associative plasticity, although in the current work only results for the associative case are presented.

3. Explicit integration of the constitutive equation

3.1. Local integration

The evolution of state variables at Gauss points adapts an explicit stress integration technique proposed by Monforte et al. (2015), which is now briefly summarized. Since an hyperelastic model is adopted the problem is framed as one of elastic deformation evolution; once the elastic strain is known the stress state is obtained just by evaluating the hyperelastic law. In this regard, the elastic Left Cauchy Green tensor in the new configuration, $\mathbf{b}^e_{n+1} = \mathbf{F}^e_{n+1} \cdot \left(\mathbf{F}^e_{n+1}\right)^T$, may be expressed, assuming an exponential approximation of the variation of the plastic deformation gradient (Simo, 1998) and employing an explicit approach (forward Euler), as:

$$\mathbf{b}^e_{n+1} = \mathbf{F}_{n+1} \cdot \mathbf{F}_n^{-1} \cdot \exp\left(-\Delta\gamma \left.\frac{\partial G(\boldsymbol{\tau}, z)}{\partial \boldsymbol{\tau}}\right|_n\right) \cdot \tag{13}$$

$$\cdot \mathbf{b}^e_n \cdot \exp\left(-\Delta\gamma \left.\frac{\partial G(\boldsymbol{\tau}, z)}{\partial \boldsymbol{\tau}}\right|_n\right)^T \cdot \mathbf{F}_n^{-T} \cdot \mathbf{F}_{n+1}^T$$

whereas the evolution of a generic strain-like hardening variable, β, is:

$$\beta_{n+1} = \beta_n + h\left(\mathbf{l}^p\right) = \beta_n + \Delta\gamma\, h\left(\left.\frac{\partial G(\boldsymbol{\tau}, z)}{\partial \boldsymbol{\tau}}\right|_n\right) \tag{14}$$

where the subscripts $n+1$ and n stands for quantities evaluated at configuration t_{n+1} and t_n, respectively.

In the previous two expressions, Equations (13) and (14), all the terms are known with the exception of the plastic multiplier increment, $\Delta\gamma$. This might be obtained as:

$$\Delta\gamma = \frac{\frac{\partial f}{\partial \boldsymbol{\tau}} : \mathbb{D}^e : \nabla^s \Delta\mathbf{u}}{H + \frac{\partial f}{\partial \boldsymbol{\tau}} : \mathbb{D}^e : \frac{\partial G}{\partial \boldsymbol{\tau}}} \tag{15}$$

where $H = -\frac{\partial f}{\partial z} \cdot \frac{\partial z}{\partial \beta} \cdot h\left(\frac{\partial G}{\partial \boldsymbol{\tau}}\right)$ is the plastic modulus, z and β stand for the stress-like and strain-like, respectively, internal variables (see Box 1) and $\nabla^s \Delta\mathbf{u}$ is the symmetric gradient of the incremental displacements.

The adopted hyper-elastic model has been formulated in terms of the elastic Hencky strain and the Kirchhoff stress. Therefore, once the elastic Cauchy-Green tensor, Equation (13), has been calculated, the stress state is obtained by first computing the elastic Hencky strain, $\boldsymbol{\epsilon}^e = \ln(\mathbf{b}^e)$, and then evaluating the hyper-elastic model.

Finally, to use the developed algorithm in the context of a Finite Element code with implicit integration of the global problem, an expression for the stiffness matrix is required; the Lie derivative of the Kirchhoff stress tensor may be expressed as:

$$\mathcal{L}_v \boldsymbol{\tau} = \left(\mathbb{D}^e - \frac{\mathbb{D}^e : \frac{\partial G}{\partial \boldsymbol{\tau}} \otimes \frac{\partial f}{\partial \boldsymbol{\tau}} : \mathbb{D}^e}{H + \frac{\partial f}{\partial \boldsymbol{\tau}} : \mathbb{D}^e : \frac{\partial G}{\partial \boldsymbol{\tau}}}\right) : \mathbf{d} \tag{16}$$

where $\mathbb{D}^e$ is the elastic stiffness matrix and $\mathbf{d} = \nabla^s \mathbf{v}$ is the symmetric part of the velocity gradient.

In the case of purely elastic straining -null increment of the plastic multiplier- Equations (13) and (16) reduce to the usual large deformation elastic update equations:

$$\mathbf{b}^e_{n+1} = \mathbf{F}_{n+1} \cdot \mathbf{F}_n^{-1} \cdot \mathbf{b}^e_n \cdot \mathbf{F}_n^{-T} \cdot \mathbf{F}_{n+1}^T \tag{17}$$

$$\mathcal{L}_v \boldsymbol{\tau} = \mathbb{D}^e : \mathbf{d} \tag{18}$$

Explicit stress integration techniques have several drawbacks: (i) the resulting stress typically may not lay in the yield surface, (ii) the accuracy of the technique is heavily influenced by the magnitude of the strain increment and (iii) special techniques are required when, in a single strain increment conditions cross from elasticity into elasto-plasticity (Potts and Gens, 1985; Sloan et al., 2001). To overcome those drawbacks, the update equations are solved by employing both a yield surface drift correction algorithm (Potts and Gens, 1985) and an adaptive substepping algorithm (Sloan et al., 2001).

In the literature, typically, two different order Runge-Kutta methods are used in the adaptive substepping algorithm (Sloan et al., 2001; Lloret-Cabot et al., 2016); the difference between both stress approximations is used to define an error measure, which is used for adjusting the time step. As noted previously, in this work the update equations have been developed only for the forward Euler method (see Equation (13)). Then, each deformation increment is computed with two different temporal discretizations: one using only one deformation increment and the other using three deformation increments. The difference between these two approximations is used as error measure in the adaptive substepping algorithm.

3.2. Nonlocal reformulation

In numerical simulations where softening is encountered, the solution typically exhibit a pathological mesh dependence, leading to unrealistic results. This numerical pathology may be mitigated by employing a nonlocal approach. This means that the constitutive model is evaluated by utilizing one or more nonlocal variables instead of their local counterpart. The expression of a nonlocal variable $\tilde{\beta}$ employing an isotropic integral type method is:

$$\tilde{\beta}(\mathbf{x}) = \frac{\int_\Omega w(\mathbf{x}, \|\mathbf{y} - \mathbf{x}\|)\, \beta(\mathbf{y})\, \mathrm{d}\Omega}{\int_\Omega w(\mathbf{x}, \|\mathbf{y} - \mathbf{x}\|)\, \mathrm{d}\Omega} \tag{19}$$

where $w(\mathbf{x},\chi)$ is the weighting function for point $\mathbf{x}$ controlling the influence of its neighbors in terms of their relative distance $\chi = \|\mathbf{y} - \mathbf{x}\|$.

This expression is typically numerically discretized, for point i, as:

$$\tilde{\beta}(\mathbf{x}_i) = \frac{\sum_j w(\mathbf{x}_i,\chi_{ij})\beta(\mathbf{x}_j)}{\sum_j w(\mathbf{x}_i,\chi_{ij})} \tag{20}$$

where $\chi_{ij} = \|\mathbf{x}_i - \mathbf{x}_j\|$ is the distance between integration points i and j.

Several expressions have been employed for the weighting function $w(\mathbf{x},\chi)$: Gaussian distributions (de Pouplana and Oñate, 2016), bell-shaped functions, which do not require a cut-off (Jin and Arson, 2018a), and that proposed by Galavi and Schweiger (2010).

The nonlocal formulation also depends on which variable or variables are chosen to be nonlocal. In the literature, several variables have been considered, such as strains, plastic strains, the rate of the plastic multiplier or hardening variables, among others (Bažant and Jirásek, 2002; Jirásek and Rolshoven, 2003).

As outlined in Table 1 (last column), in this work three strain-like hardening parameters are treated as nonlocal variables, namely ϵ_v^p, $\bar{\epsilon}_v^p$ and α, defined in Equations (9) and (10). Afterwards stress-like hardening variables (p_s, p_t and p_m) are directly computed by evaluating Equations (11) and (12). The weighting function proposed by Galavi and Schweiger (2010) is employed here as it has been found to outperform other weighting functions in removing the mesh bias (Summersgill et al., 2017a; Mánica et al., 2018). This weighing function may be expressed:

$$w(\mathbf{x},\chi) = \frac{\chi}{l_c}\exp\left(-\left(\frac{\chi}{l_c}\right)^2\right) \tag{21}$$

where l_c is the characteristic length introduced by the averaging function. This function is equal to zero for $\chi = 0$ and maximum for $\chi = \sqrt{2}\,l_c/2$. Thus, values of the local variables at a Gauss point do not influence its nonlocal counterpart; meanwhile, their influence is maximum for points located at a distance $\sqrt{2}\,l_c/2$.

When nonlocal models are used for regularization purposes the characteristic length is usually conceived of as a numerical artifact to introduce a length scale to the constitutive behavior and to the solution (Summersgill et al., 2017b). However, even if the characteristic length does not necessarily reflect univocally an intrinsic material length -the thickness of shear bands observed experimentally, say- the selection of characteristic length values should also take into account the constitutive model and be calibrated alonside other parameters (Mánica et al., 2018).

The availability of computational resources also play a role in the definition of the characteristic length (Galavi and Schweiger, 2010; Mánica et al., 2018), because a sufficient number of neighbor Gauss points in the area where the weighting function is significantly larger than zero are required to obtain a reliable solution.

Algorithm 1 Pseudo-code for the numerical implementation of the nonlocal problem using a time split approach.

$n = 0$
while $n\,\Delta t < T_{end}$ **do**
1-. Evaluate the nonlocal internal variables:
$${}_n\tilde{\epsilon}_v^p = \frac{\int w\,{}_n\epsilon_v^p\,\mathrm{d}\Omega}{\int w\,\mathrm{d}\Omega}$$
$${}_n\tilde{\bar{\epsilon}}_v^p = \frac{\int w\,{}_n\bar{\epsilon}_v^p\,\mathrm{d}\Omega}{\int w\,\mathrm{d}\Omega}$$
$${}_n\tilde{\alpha} = \frac{\int w\,{}_n\alpha\,\mathrm{d}\Omega}{\int w\,\mathrm{d}\Omega}$$
2-. Evaluate the stress-like variables:
$${}_n\tilde{p}_s = p_{s_0}\,\exp\left(\rho_s\left({}_n\tilde{\epsilon}_v^p + \chi_s\sqrt{\tfrac{2}{3}}\,{}_n\tilde{\alpha}\right)\right)$$
$${}_n\tilde{p}_t = p_{t_0}\,\exp\left(\rho_t\left({}_n\tilde{\bar{\epsilon}}_v^p + \chi_t\sqrt{\tfrac{2}{3}}\,{}_n\tilde{\alpha}\right)\right)$$
3-. Solve the governing equations with a suitable solver for local elasto-plasticity. At each Gauss point, the constitutive model is evaluated as:
$$\left[{}_{n+1}\boldsymbol{\sigma},\ {}_{n+1}\underline{\epsilon}_v^p,\ {}_{n+1}\underline{\bar{\epsilon}}_v^p,\ {}_{n+1}\underline{\alpha}\right] = \ldots$$
$$\text{StressIntegration}\left(\mathbf{F}_n,\ \mathbf{F}_{n+1},\ {}_n\tilde{\epsilon}_v^p,\ {}_n\tilde{\bar{\epsilon}}_v^p,\ {}_n\tilde{\alpha},\ {}_n\tilde{p}_s,\ {}_n\tilde{p}_t\right)$$
4-. Once convergence is achieved, update the local variables:
$${}_{n+1}\epsilon_v^p = {}_n\epsilon_v^p + \left({}_{n+1}\underline{\epsilon}_v^p - {}_n\,\tilde{\epsilon}_v^p\right)$$
$${}_{n+1}\bar{\epsilon}_v^p = {}_n\bar{\epsilon}_v^p + \left({}_{n+1}\underline{\bar{\epsilon}}_v^p - {}_n\,\tilde{\bar{\epsilon}}_v^p\right)$$
$${}_{n+1}\alpha = {}_n\alpha + \left({}_{n+1}\underline{\alpha} - {}_n\,\tilde{\alpha}\right)$$
$n = n + 1$
end while

3.3. Numerical implementation of nonlocal effects

The numerical implementation of most nonlocal elasto-plastic models might be somewhat cumbersome, since, strictly speaking, the inclusion of the nonlocal strategy couples the constitutive response of all the Gauss points of the entire finite element mesh. As such, stress integration would no longer involve an isolated strain-driven routine to be solved at each integration point but instead would become a very large system of coupled equations that couples the constitutive behavior of all the integration points of the mesh.

To save computational resources, it is customary to solve nonlocal elasto-plastic problems by employing a time split approach (Rolshoven, 2003; Mánica et al., 2018). This approach is based on a temporal relocalization during stress point integration. Variables are computed considering nonlocal effects once at the beginning of each loading increment but, during the solution of the governing equations, they evolve independently of its neighbors. By doing so stress integration becomes again a small, independent problem at each Gauss point, preserving the usual strain-driven form and requiring minimal modifications to an already existing code for the local problem.

Algorithm 1 presents the pseudo-code developing such approach for the constitutive model employed in this work. Once the nonlocal variables are evaluated by geometrical averaging of their local counterpart, nonlocal stress-like hardening parameters are explicitly evaluated from the internal variables, Equations (11) and (12). Then, the governing equations are solved using a suitable solver for the local problem, but (at each Gauss

point) employing the nonlocal variables in the stress integration model. After equilibrium is reached, local variables are updated with their increment during that solution step. This process is repeated for each loading or displacement increment.

4. IMPLEX integration

The convergence of the Newton-Raphson procedure of the global problem depends, for instance, on the time step, but, most importantly, on the spectral properties of the resulting tangent matrix (Oliver et al., 2008). In problems that involve a large amount of softening, the convergence of the global problem may be challenging because the tangent matrix becomes singular or ill-conditioned at certain stages of the simulation. This problem may be aggravated by the use of a nonlocal plastic model, as it may increase the number of negative eigenvalues of the stiffness matrix with respect to its local counterpart (Lu et al., 2009). Therefore, very small time-steps and a large number of iterations may be required to attain convergence of the global problem (if possible).

Oliver et al. (2008) presented an integration scheme (IMPLEX integration) for non-linear constitutive models whose aim is to provide additional computability and robustness and reduce the computational cost in the analysis of Solid Mechanics problems. The algorithm may be summarized as a two step solver with a prediction or extrapolation step and a correction step. In the case of elasto-plastic problems, the first step (extrapolation step) consists on computing the boundary value problem using an extrapolated value of the increment of the plastic multiplier; that is, the magnitude of plastic strains are assumed beforehand. In the second step (correction step) the constitutive equations are correctly evaluated at each integration point using the displacement field obtained in the extrapolation step; the resulting increment of the plastic multiplier is used in the next extrapolation step.

An important property of the IMPLEX technique is that, for a set of constitutive models, the global problem becomes step-linear: that is, the iterative solving process converges in a unique step (Oliver et al., 2008; Sánchez et al., 2008). For the rest of constitutive models or in cases where the governing equations are formulated using the concept of large strains, the number of iterations required to converge the global problem drastically decrease with respect to usual algorithms. This benefit, due to the extrapolative nature of the technique, comes with a price: each IMPLEX iteration introduces some error to the solution that depends on the size of the time step (Titscher et al., 2019).

In the original proposal of the method, the equations for the evaluation of the constitutive response in the extrapolation step (with an assumed increment of the plastic multiplier) and the correction step are discretized employing an implicit approach (Oliver et al., 2008; Titscher et al., 2019). This is not the only possibility, for instance, Prazeres et al. (2016) employed an explicit approach for the extrapolation step.

In this work, both evaluations of the constitutive model use explicit approaches. In the extrapolation step, the model is integrated explicitly in a single step. In the correction step, stresses are evaluated using the previously introduced explicit stress integration technique, including adaptive substepping and yield surface drift correction.

4.1. Extrapolation step

In the extrapolation step, the governing equations are solved by evaluating the constitutive model with a plastic multiplier known beforehand, $\overline{\Delta\gamma}$; they are thus independent of the displacements. Following the Modified IMPLEX method developed by Prazeres et al. (2016), an explicit equation is employed for the extrapolation step. The elastic deformation in the new configuration -the IMPLEX counterpart of Equation (13)- is then expressed as:

$$\mathbf{b}^e_{n+1} = \mathbf{F}_{n+1}\cdot\mathbf{F}_n^{-1}\cdot\exp\left(-\overline{\Delta\gamma}\ \left.\frac{\partial G(\boldsymbol{\tau},z)}{\partial\boldsymbol{\tau}}\right|_n\right)\cdot \tag{22}$$

$$\cdot\mathbf{b}^e_n\cdot\exp\left(-\overline{\Delta\gamma}\ \left.\frac{\partial G(\boldsymbol{\tau},z)}{\partial\boldsymbol{\tau}}\right|_n\right)^T\cdot\mathbf{F}_n^{-T}\cdot\mathbf{F}_{n+1}^T$$

and the internal hardening variables:

$$\beta_{n+1} = \beta_n + \overline{\Delta\gamma}\,h\left(\left.\frac{\partial G(\boldsymbol{\tau},z)}{\partial\boldsymbol{\tau}}\right|_n\right) \tag{23}$$

It is important to emphasize that in the previous two expressions all the quantities are known with the exception of the deformation gradient at the new configuration, $\mathbf{F}_{n+1}$, that is retrieved solving by the global problem.

During the extrapolation step the linearized material stiffness matrix becomes:

$$\mathcal{L}_v\boldsymbol{\tau} = \mathbb{D}^e : \mathbf{d} \tag{24}$$

that is, it coincides with the elastic stiffness matrix since in Equation (22) the terms related to plastic flow are assumed beforehand (i.e, the plastic flow is assumed beforehand and independent of the displacement field). Therefore, by employing this modified IMPLEX technique the global problem has the same formal structure than an elastic problem.

4.2. Correction step

During the correction step, the constitutive model is evaluated (at each integration point) employing the usual elasto-plastic constitutive model, where the increment of strain that is integrated is that obtained in the extrapolation step. The increment of plastic multiplier that will be used in the subsequent extrapolation step ($\overline{\Delta\gamma}$) is that obtained in this correction phase.

5. Application to single-element tests

The performance of the explicit and the IMPLEX integration algorithms is first tested by simulating a series of laboratory tests (oedoemeter and drained triaxial tests). To assess the convergence rate of the numerical solution, these problems are computed with several step sizes. Due to the complexity of the constitutive model, no closed-form solution exists for the evolution of stress and strains during loading; therefore, a reference solution is obtained using a very large number of steps (one

Table 2: Constitutive parameters adopted in this work

Section	E (kPa)	ν	M	k	p_s (kPa)	p_t (kPa)	ρ_s	ρ_t	χ_s	χ_t
5: Elementary tests	$5 \cdot 10^4$	0.2	1.4	5	1200	320	16.6	-30.0	0	0.5
6.2: Biaxial tests	$5 \cdot 10^4$	0.2	1.4	5	500	50	16.6	-15.0	0	0.3
6.3: Footing indentation	$5 \cdot 10^4$	0.2	1.4	5	500	100	16.6	-15.0	0	0.5

million steps). For stresses, the relative error may be defined as:

$$\text{Error}_\sigma = \sqrt{\frac{||\boldsymbol{\sigma} - \boldsymbol{\sigma}^\star||^2 + ||\mathbf{z} - \mathbf{z}^\star||^2}{||\boldsymbol{\sigma}^\star||^2 + ||\mathbf{z}^\star||^2}} \tag{25}$$

where $\mathbf{z} = [p_s,\, p_t,\, p_c^\star]$ are the stress-like hardening variables and $\boldsymbol{\sigma}^\star$ stand for values obtained from the reference solution.

Meanwhile, for the Hencky strain, $\boldsymbol{\epsilon} = \ln\left(\mathbf{F} \cdot \mathbf{F}^T\right)$, the error is measured as:

$$\text{Error}_\epsilon = \frac{||\boldsymbol{\epsilon} - \boldsymbol{\epsilon}^\star||}{||\boldsymbol{\epsilon}^\star||} \tag{26}$$

where, again, $\boldsymbol{\epsilon}^\star$ is the reference Hencky strain and $\boldsymbol{\epsilon}$ is the solution obtained with a finite number of steps.

The constitutive parameters of all the simulations of this section are given in Table 2. Although this parameter set has not been calibrated to represent any specific material, the values in Table 2 are within the range employed in previous work (Arroyo et al., 2005; Tamagnini and Ciantia, 2016) to simulate the behavior of calcarenites, which are highly porous soft carbonate rocks. Finally, the initial stress state is characterized by $p' = 120$ kPa and $q = 0$ kPa.

5.1. Oedometer test

The first example is an oedometric test. It corresponds to a strain-driven problem; thus, only the explicit stress integration scheme is considered, since the IMPLEX technique is only relevant in cases where a non-linear system of equations needs to be solved. The total vertical strain increment is applied in a number of equal strain increments, ranging from 6 to 10^6, which is taken as the reference solution.

Figure 2 characterizes the stress path of the problem. During the elastic regime, the trajectory of the stress path is governed by the Poisson's ratio of the soil. Once the stress strain reaches the yield surface the soil suffers from severe softening due to destructuration; at the same time, the preconsolidation pressure of the reconstituted soil, p_s, increases. Once the effect of the structure has been erased ($p_t = 0$), the soil hardens. During the whole problem, the soil experience compressive volumetric strains (Figure 2(b)).

Figure 3 presents the convergence analysis; the slope of this curve is close to 1; this is in line with the expected performance of a first-order accurate algorithm, such as the forward Euler employed in this work (Tamagnini and Ciantia, 2016; Sołowski and Sloan, 2014). A plateau is observed for the cases computed between 20 and 100 steps; in this region the error is in the order of 10^{-5} and it is related to the tolerance imposed in the substepping algorithm. For cases computed with less than 20 steps, the convergence curve exhibits again a linear tendency and the error increases again, more steeply. In this region the substepping scheme computes several increments with the imposed minimal increment size without converging, thus adding error to the solution.

5.2. Drained triaxial test

The second example corresponds to a drained triaxial test. This test requires mixed control conditions (i.e. imposed strain and stress increments) and, thus, a nonlinear system of equations has to be solved each loading step, which is done following a similar rational than that proposed by Bardet and Choucair (1991). During the solution of this nonlinear system the IMPLEX technique may be also applied instead of the preestablished explicit integration algorithm. This allows an initial assessment of this technique in this simple single-element setting.

Figure 4(a) presents the stress path and also the evolution of the stress-like plastic variables. The solid black curve represents the initial yield surface and the dotted black curve the initial reference surface (i.e. the yield surface of the unstructured soil). Once the soil reaches the initial yield surface, its size gradually decreases due to the combined effects of destructuration and dilatancy, until it reaches a critical state. Brittleness in mechanical response is showcased in Figure 4(b) depicting the evolution of the deviatoric stress, $q = \sigma_1 - \sigma_3$, in terms of the axial Hencky strain. First, deviatoric stresses increase in elastic regime until the soil yields, when deviatoric stresses sharply reduce.

When using the explicit stress integration scheme, the results show little influence of the number of time-steps used to compute the solution (see Figure 4). This can be also seen in the convergence analysis reported in Figure 5, where the slope of the convergence curve in terms of stresses and strains is slightly larger than 1, in good agreement with the expected convergence rate of a first-order accurate algorithm.

Larger errors are generally obtained with the application of the IMPLEX technique, particularly at low step numbers. At this stage it would therefore seem then that the application of the IMPLEX technique is superfluous or even counterproductive. However, this is just because the most important benefit derived from the IMPLEX technique -a tangent matrix with positive eigenvalues- does only enter into play when addressing boundary value problems, as will be shown in the next section.

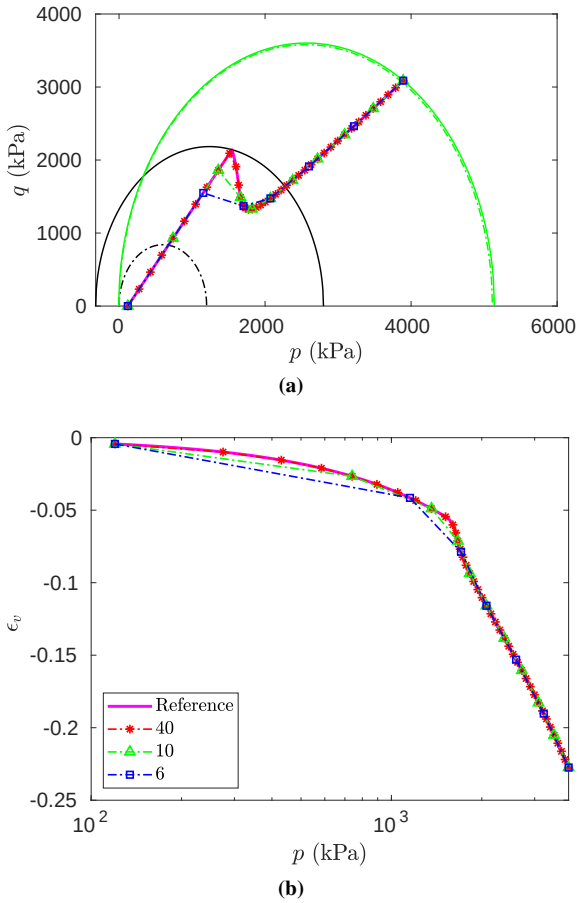

Figure 2: Strain-controlled oedometer test. Stress trajectory in the $p-q$ plane, (a), and $\epsilon_v - p$ plane, (b). Results are labeled by the number of increments used to compute the solution; the reference solution is obtained with one million steps

. In (a), the initial yield surface is depicted in black whereas the final one in green.

6. Application to boundary value problems

A number of two-dimensional analyses are reported to assess the performance of the developed numerical algorithms alongside of the constitutive model. The first set of numerical simulations correspond to biaxial tests, which are used to showcase the mesh-independence properties of the nonlocal approach and to compare both stress integration schemes in a boundary value problem. Secondly, in order to demonstrate the ability of developed algorithms to handle problems involving large deformations, the insertion of a rigid footing is presented. Whilst for the biaxial compression tests the material is considered to be dry, the rigid footing simulations will consider transient coupled hydro-mechanical conditions.

6.1. G-PFEM

This work uses the numerical code G-PFEM (Geotechnical Particle Finite Element Method), which has been specifically developed for the analysis of large strain contact problems in geomechanics (Monforte et al., 2017, 2018). G-PFEM is implemented into Kratos Multiphysics framework (Dadvand et al., 2010), an object-oriented multi-disciplinary open-access platform for numerical analysis tool development.

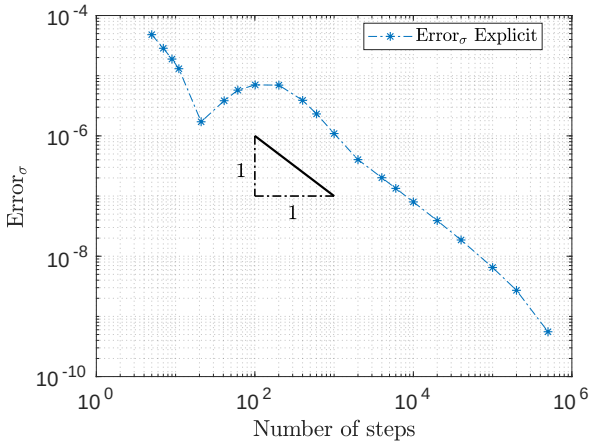

Figure 3: Oedometer test. Evolution of the relative error of stresses, Error_σ, in terms of the number of steps.

The Particle Finite Element method (PFEM) is a Lagrangian numerical technique suitable for large deformation problems; PFEM combines the standard FEM with an efficient remeshing algorithm (Oñate et al., 2004). A particularity of PFEM is that only low order elements are used -linear triangle in 2D and linear tetrahedrons in 3D- and the governing equations are written in an Updated Lagrangian approach. The method has been applied to a variety of multi-physics problems, ranging from its original proposal to fluid-structure interaction (Idelsohn et al., 2004; Oñate et al., 2008; Franci et al., 2015) to geomechanics (Larese et al., 2008; Carbonell et al., 2013; Zhang et al., 2014; Monforte et al., 2017, 2018).

A typical solution algorithm involves the following steps (Oñate et al., 2004):

1. Discretize the domain with a Finite Element mesh,
2. Identify the external boundaries and apply the boundary conditions,
3. Compute some time-steps of the problem,
4. Construct a new mesh and interpolate state variables between the previous mesh and the new one with suitable algorithms,
5. Go back to step 2 and repeat the solution process for the next time-steps.

An additional feature of the original algorithm is the resource to *h*-adaptive techniques and mesh smoothing technique (see Rodríguez et al., 2016, 2017, for further details). This feature is relevant here, since *h*-adaptive techniques refine the discretization in areas where localization takes place. This is particularly convenient for the nonlocal approach, because for it to be effective nonlocal variables should be computed with a sufficient number of neighboring Gauss points (Galavi and Schweiger, 2010). The use of nonlocal approaches in conjunction with *h*-adaptive techniques has been repeatedly advocated by various researchers using damage models (Rodríguez-Ferran and Huerta, 2000; Rodríguez-Ferran et al., 2004; de Pouplana and

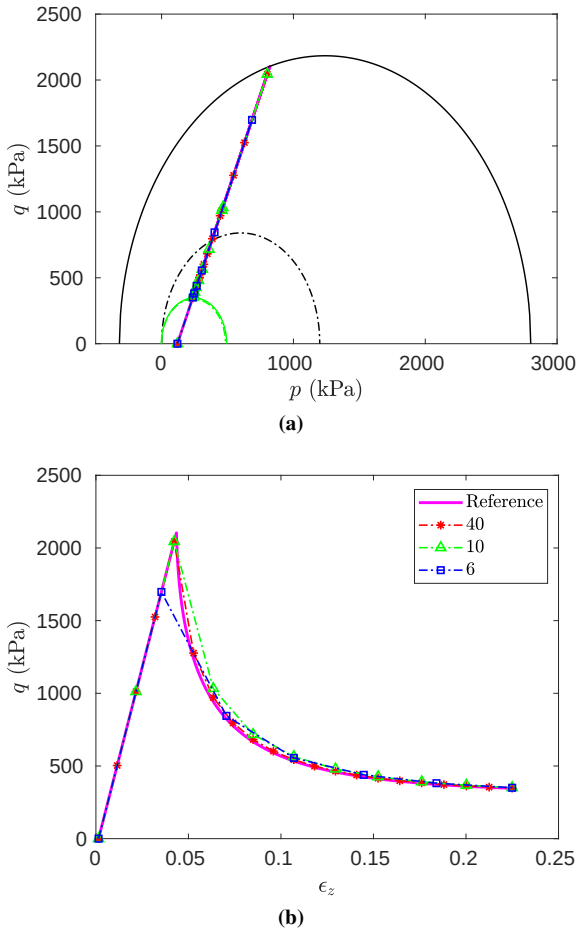

Figure 4: Drained triaxial test. Stress trajectory in the $p - q$ plane, (a), and $\epsilon_z - q$ plane. Results are labeled by the number of increments used to compute the solution; the reference solution is obtained with one million steps. In (a), the initial yield surface is depicted in solid black whereas the final one in green.

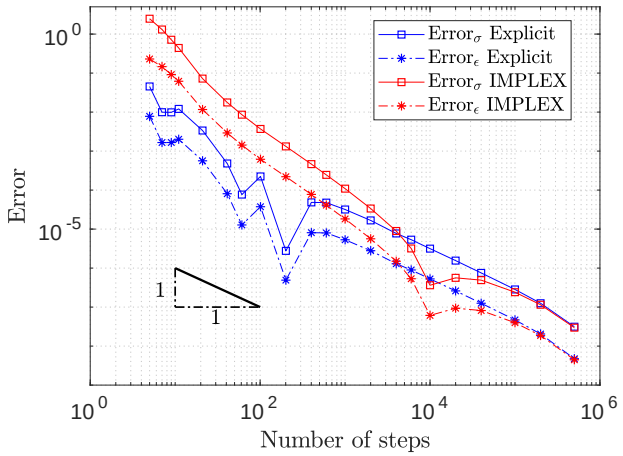

Figure 5: Drained triaxial test. Evolution of the relative error, Error_σ and Error_ϵ, in terms of the number of steps for the Explicit and the IMPLEX integration techniques.

Oñate, 2016). Indeed, since the failure pattern is generally not known a priori, nonlocal approaches that rely on a fixed mesh are penalized by the need to lay out a very fine discretization (Mánica et al., 2018; Summersgill et al., 2017a).

In this work, the refinement criterion used in the h-adaptive routines is the product of the accumulated plastic shear strain, α, and the area of the element. Only elements that reach a critical value are refined. Elements might be continuously refined until a specified minimum element size, h_c, is reached. This minimum element size, h_c, is defined as a fraction of the characteristic length of the nonlocal model, l_c. By using this approach, the region of strain softening is automatically identified and the element resolution is increased so that a sufficient number of Gauss points exists to accurately evaluate nonlocal variables.

As already mentioned, only linear triangular elements are used in PFEM. Therefore, in the case of the hydromechanical problem, displacements and water pressure are discretized with the same shape functions, which is known to cause instabilities in the undrained limit (Pastor et al., 1999; Monforte et al., 2019); thus, the mass conservation equation of the byphasic medium is stabilized with the Polynomial Projection technique (Bochev et al., 2006; Monforte et al., 2017, 2018).

6.2. *Biaxial tests*

In this set of numerical simulations, unstructured triangular meshes are employed with all the nodes equally distributed. The occurrence of strain localization may lead to distortion of elements and local concentration of nodes in the same region. The PFEM algorithms are applied to keep the quality of the mesh but without sharply varying the number of elements and nodes in the discretization; thus, without using yet the h-adaptive part of the algorithms.

The meshes employed are illustrated in Figure 6 in the initial and final configurations. The width of the domain is equal to $B = 0.1$ m whereas the height is $H = 1.75\,B = 0.175$ m. At the top boundary, a prescribed downwards vertical displacement equal to $0.1H$ (a tenth of the original height) is imposed whereas horizontal displacements are null. Meanwhile, null displacements in all directions are imposed on the bottom boundary. This simulates a biaxial cell with perfectly rough platens, to develop the non-homogeneous stress field that will trigger strain localization. The vertical displacement at the top is applied in a number of equal increments, different in magnitude for different simulations. The soil constitutive parameters are listed in Table 2 (second row), and the characteristic length of the nonlocal approach is set to $l_c = 0.15\,B = 0.015$ m.

6.2.1. *Robustness and efficiency of stress integration procedures*

Prior to analyze the mesh dependence of the solution, a base case is computed with Mesh A, composed by 602 nodes and 1100 triangular elements (Figure 6). Results obtained using the nonlocal formulation, using both the IMPLEX and the explicit stress integration approach, are presented in Figure 7. The same problem has been computed repeatedly, employing a different number of equal displacement increments. Results are reported

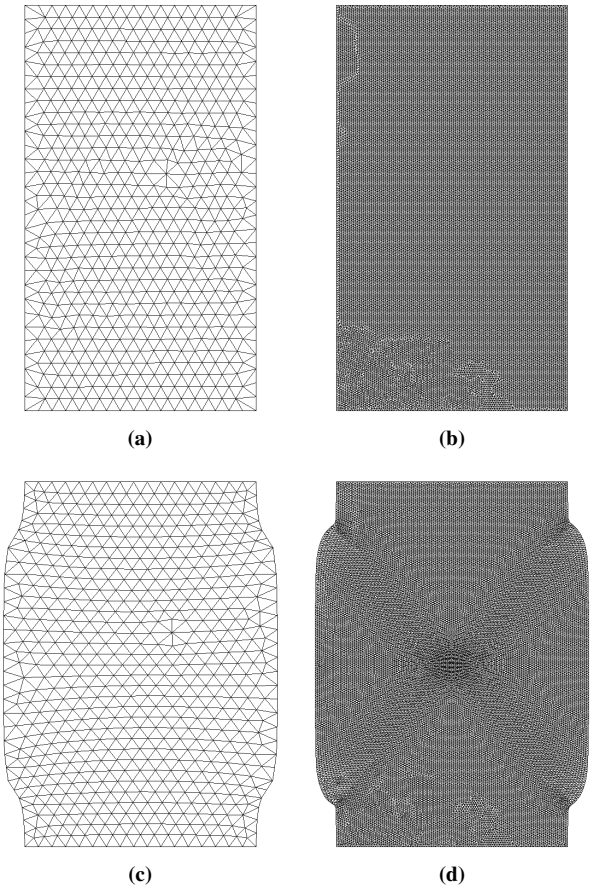

Figure 6: Biaxial test. Mesh A, (a) and (c), and Mesh F, (b) and (d), at the beginning and end of the problem; see Table 4.

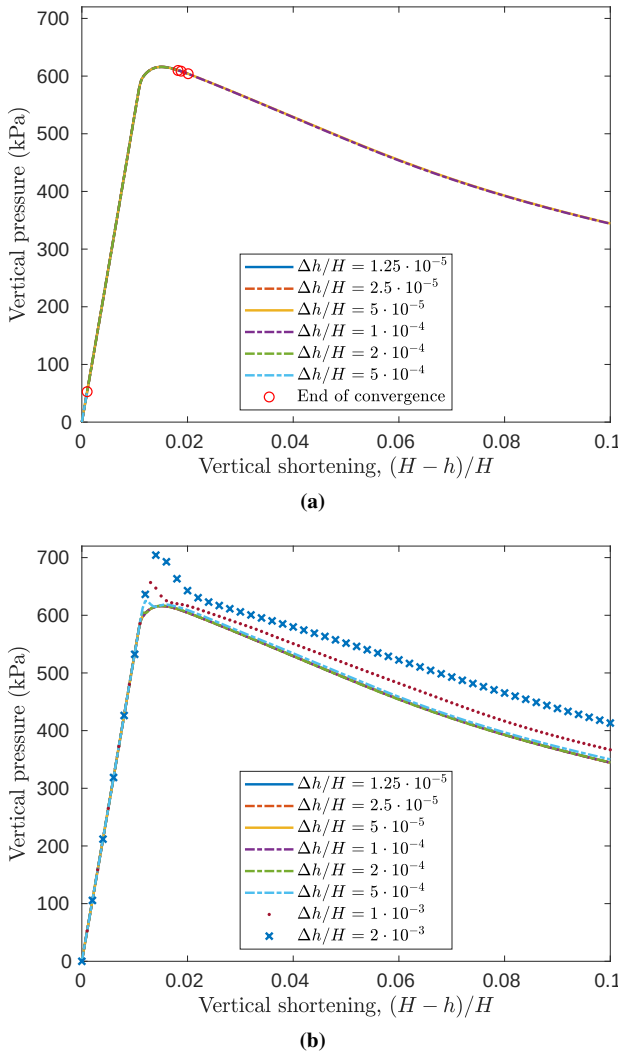

Figure 7: Biaxial test. Evolution of the vertical pressure imposed at the top plate in terms of the axial deformation for different stress integration approaches: explicit approach, (a), and Implex scheme, (b). The lack of convergence on some simulations is indicated with a red circle.

in terms of nominal engineering strain, given by the ratio of incremental displacement imposed at the top boundary, Δh, normalized by the initial height of the specimen, H.

The nonlocal algorithm does not degrade the step-independence of the explicit stress integration results (see Figure 7(a)). However, the drawback is also clear: most simulations could not continue until the specified final displacement due to numerical divergence in the global problem. For instance, in the case with the lowest value of increments, the solution diverges at the fourth time step, which is indicated with a circle in the load-displacement curve presented in Figure 7(a)). This is partly a consequence of the high non-linearity of the global problem but also of the appearance of negative eigenvalues in the system of nonlinear equations to be solved.

On the contrary, the robustness of the IMPLEX technique is demonstrated, since all the cases converged until the final displacement was attained, even for the smallest number of displacement increments. This is a consequence of the extrapolative nature of the technique: the stiffness matrix has the same formal structure than an elastic problem, thus the tangent matrix is always symmetric and positive definite.

Due to the different nature of the local stiffness matrix, the number of iterations to solve the global problem is also different. By using the IMPLEX technique less than 4 iterations are required to achieve the desired tolerance whereas more than 10 are needed in the explicit approach. Consequently, the IMPLEX technique also reduces the computational cost. This is shown in Table 3, where the computational costs of the two techniques are compared for cases in which the prescribed final displacement was attained. As shown, the IMPLEX scheme is more than four times faster than explicit stress integration.

Again, using the IMPLEX technique with a very low number of loading increments may introduce errors in the solution (see Figure 7). However, once a sufficient number of steps is employed, the influence of the time discretization error is largely mitigated.

6.2.2. Mesh independence

In this section mesh independence is evaluated considering examples for which the number of steps is such that the Implex based stress integration is equivalent to the explicit technique.

Table 3: Biaxial test. Computational cost using the explicit integration scheme, t_{expl}, and the Implex technique, t_{implex}, for different number of steps, n_{steps}. Mesh A. Cases with spontaneous numerical break-down are marked with a "-".

$\Delta h/H$	n_{steps}	t_{expl} (s)	t_{implex} (s)	Speed-up
$1.25 \cdot 10^{-5}$	8000	-	1811.1	-
$2.5 \cdot 10^{-5}$	4000	-	962.6	-
$5 \cdot 10^{-5}$	2000	2432.8	531.18	4.58
$1 \cdot 10^{-4}$	1000	1543.4	327.13	4.72
$2 \cdot 10^{-4}$	500	-	182.79	-
$4 \cdot 10^{-4}$	250	-	105.42	-

To this end, the biaxial test of the previous section is computed with several Finite Element meshes, whose metrics are defined in Table 4; the finest and coarsest discretizations are also shown in Figure 6 at the beginning and end of the simulation.

Figure 8 depicts the results of the biaxial tests obtained by either employing the nonlocal approach or not. It is remarkable how the nonlocal approach is capable of alleviating the pathological mesh-dependency of softening in the Finite Element methods. Numerical results still show a small mesh-dependency for the nonlocal approach (Figure 8), of a similar relative magnitude to that observed in previous works (Summersgill et al., 2017a,b).

The load-displacement curves of both local and nonlocal computations indicate that, in most instances, the rate of softening is controlled by element size. However, the coarser mesh (Mesh A) does not seem to agree with this tendency. This fact may be attributed to slight differences in the preferential mesh alignment between meshes: Pastor and Quecedo (1995) demonstrated that mesh alignment has a paramount importance on the failure mechanism in simulations involving low order finite elements and softening, such as in this work. An in-depth examination of the complex interplay between remeshing, preferential alignment and nonlocal model evaluation algorithms is a worthy topic for further research, but out of the scope of this work.

Figure 9 presents the (local) accumulated plastic deviatoric strain, α, (defined in Equation (10)) and the vertical component of the Green-Lagrange strain tensor, computed using the nonlocal approach for all the Finite Element discretizations. All the simulations present the same failure mechanism and the resolution of the plastic variables increases with the number of elements of the discretization. Figure 9 clearly shows that, independently from the finite element mesh used, the thickness of the shear band is very similar to the length scale parameter, l_c (see Figures 6 and 9); this result is consistent with previous research on nonlocal implementations of other elasto-plastic constitutive models (Galavi and Schweiger, 2010; Mánica et al., 2018).

6.3. Indentation of a rigid strip footing

The last example selected to showcase the proposed numerical approach simulates the indentation of a rigid, strip footing in

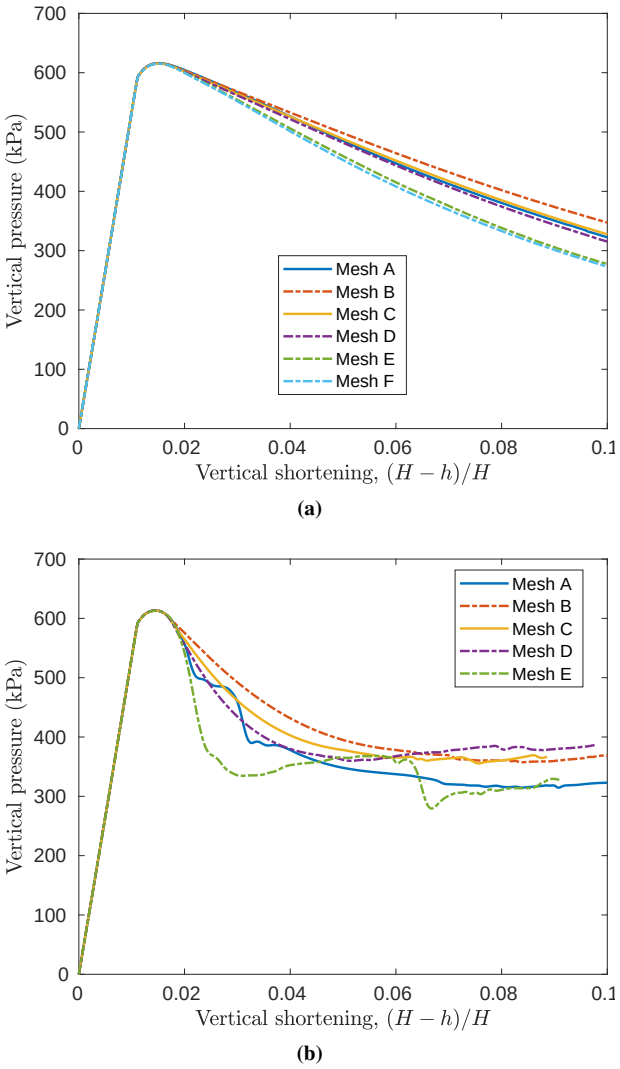

Figure 8: Biaxial test. Mesh sensitivity. Evolution of the vertical pressure imposed at the top plate in terms of the axial deformation for different Finite Element meshes using a nonlocal approach, (a), and local elasto-plasticity model, (b).

a porous soft rock. In this example a fully coupled hydromechnical analysis is performed and permeability is varied by six orders of magnitude in the simulations, to cover the full spectrum of behavior from drained to undrained conditions. The geometry of the problem may be seen in Figure 10, which reports the initial Finite Element mesh at the end of the problem. Vertical symmetry is applied to reduce the problem size. The domain expands 10 B in the horizontal direction and 7.5 B in the vertical direction, being B the width of the footing that is equal to 2m. Both displacements are restricted in the lower boundary, whereas null horizontal displacements are imposed in the vertical boundaries; null excess water pressure is imposed at the free surface. The footing is considered fully rigid and its interface with the soil completely rough (i.e. perfect adherence). A footing indentation rate of $B/2$ per day is assumed.

All the simulations of this subsection are obtained using the IMPLEX technique with the nonlocal elasto-plastic model.

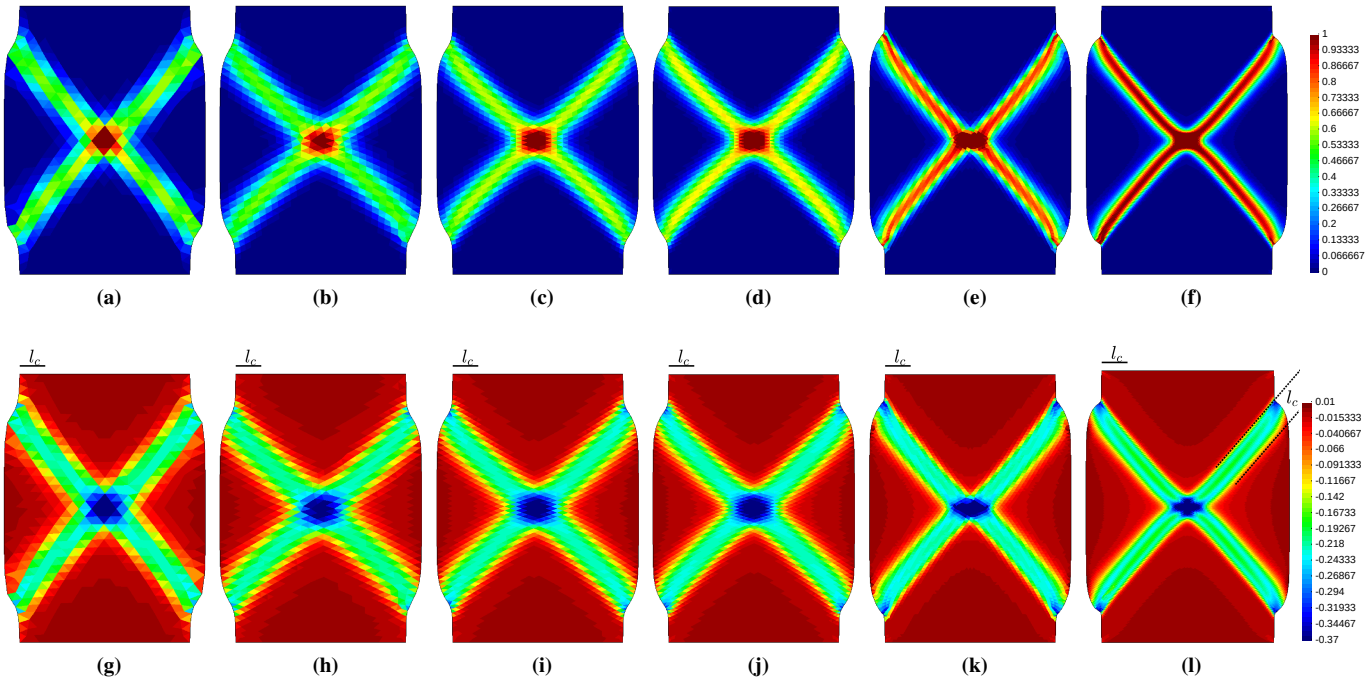

Figure 9: Biaxial test. On top, accumulated plastic deviatoric strain, α, (defined on Equation (10)). On the bottom, vertical component of the Green-Lagrange strain tensor. The number of elements increases from left to right, see Table 4.

Table 4: Initial number of nodes and elements, in terms of the element characteristic size h_e, of the meshes employed in the mesh-dependency analysis.

Mesh	Number of nodes	Number of elements
A	602	1100
B	1037	2474
C	2289	4394
D	3302	6382
E	5122	9968
F	20320	40088

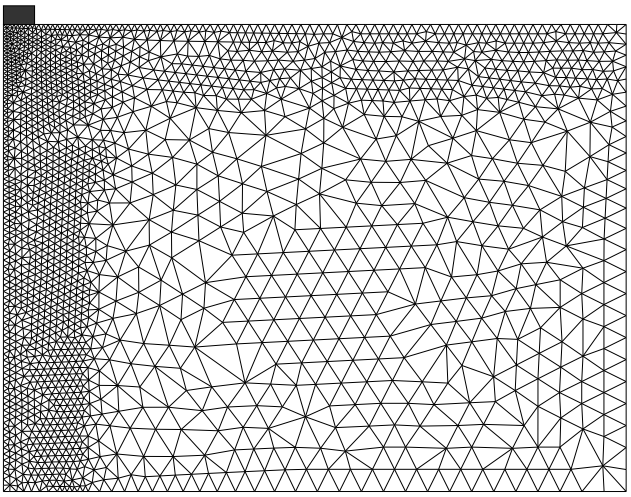

Figure 10: Rigid, strip footing. Initial finite element mesh.

Also all the remeshing capabilities of G-PFEM are enabled. Whilst in the previous sections, the PFEM algorithms to insert or eliminate nodes were just used to maintain the quality of the Finite Element mesh additional h-adaptive meshing routines are here employed (Carbonell et al., 2013; Rodríguez et al., 2016). Therefore, new nodes are inserted in areas were plastic flow is large; in particular the value of is employed as a mesh-refinement criterion.

The constitutive parameters are reported in Table 2 (last row), and assumed homogeneous along the whole domain. In this set of simulations soil self weight is also considered; the initial stress profile is constructed with $K_0 = 0.5$. The characteristic length of the nonlocal model is set as $l_c = 0.025B$.

Figure 11 presents the footing penetration curves for different values of permeability. All the simulations show similar overall behaviour: a stiff initial elastic response until a fairly marked structural yielding takes place at around 1350 kPa. The post yield behaviour, on the other hand, is highly dependent on permeability. For the two lowest permeability values the applied footing pressure does not increase post-yield, but rather decreases, with a sudden collapse at a footing indentation close to $0.14\,B$ breaking a plastic plateau. For the two larger permeabilities the footing shows structural hardening and, despite some jumps, the applied pressure increases during penetration.

These structural responses are partly clarified in Figure 12 where several field variables (pore water pressure, the bonding related plastic internal variable and the accumulated plas-

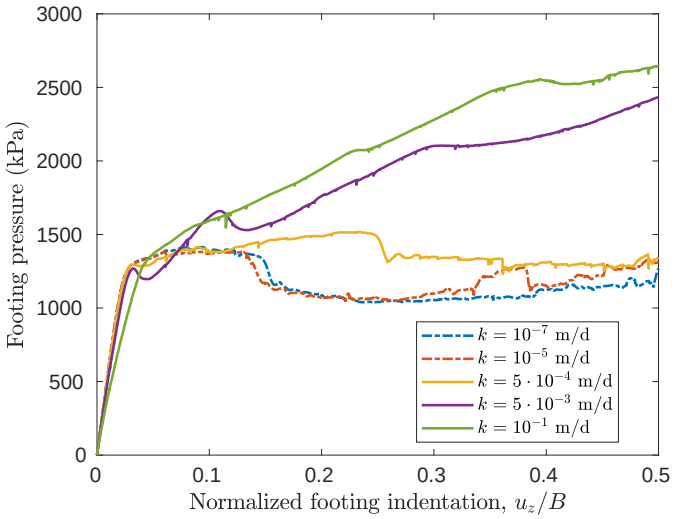

Figure 11: Rigid, strip footing. Curve of the footing resistance in terms of the normalized indentation for different soil permeabilities, expressed in meters per day.

tic shear strain, α), are plotted at the final simulation stage - corresponding to a footing indentation of $0.5\,B$. For instance, the pore pressure field shows that, for the larger permeability the footing penetration is practically drained. For lower permeability a significant bulb of positive excess pore pressure appears beneath the footing, reducing in size but increasing in pressure as the material becomes more impermeable. For the lower permeabilities the overpressure bulb is accompanied by bands of underpressure that go towards the surface.

The accumulated plastic shear strain plots confirm that the underpresurized bands correspond to shear bands, where dilation is taking place. For the impermeable cases the localized shear bands define a shearing mechanism, reminiscent of classical bearing capacity. It is interesting to note that, in the case with the lowest permeability, the drop of resistance in the load-displacement curve of the footing (Figure 11) that appears at $0.14\,B$ corresponds to the moment where the full failure mechanism is formed and along these shear bands all the resistance due to the soil structure is lost ($p_t \approx 0$).

In the two cases with highest permeabilities, a punching-type failure mechanism appears. In the plastic bulb beneath the footing the material structure is completely degraded (the variable p_t is much lower than the initial one), whereas all the rest of the soil mass remains in intact conditions; qualitatively, this in accordance with physical evidences for circular footings in soft highly porous rocks (Ciantia et al., 2018; Ciantia, 2018)

The remeshing routines employed maintain a coarse mesh in most areas in elastic regime but decrease the element size in zones with plastic shearing. The remeshing is clearly visible in Figure 13, where the finite element mesh at the end of penetration is represented.

7. Conclusions

A large range of fine grained natural and artificial geomaterials exhibit more brittleness in compression than observed in the reconstituted analogues that are often used to model them in the laboratory and that inspire reference constitutive models, such as Cam-clay. Brittleness is conducive to localization and, in turn, localization leads to numerical problems. Thus, it is necessary to ensure numerical robustness to extend simulation capabilities into the post-yield range for structured soils and soft rocks.

This work has presented a numerical strategy in which several techniques are combined towards that goal. The Particle Finite Element Method (PFEM) has the advantage of facilitating the link to well-established FEM techniques, like mixed field formulations or stabilization procedures for low-order elements (Monforte et al., 2017, 2019)). Here this advantage has been exploited again to incorporate:

- a constitutive model which is representative of a wider and successful family of structure-enhanced constitutive models -with applications to natural clays, cemented soils and rocks- reformulated for large strains, something that, to the best of our knowledge, had not been attempted before for this constitutive family.

- a nonlocal integral type reformulation of the model to avoid the pathological mesh-dependence that may accompany strain localization.

- an IMPLEX integration scheme, which provides extra robustness that is required when addressing localized failure.

All this numerical technology has been applied to a number of numerical simulations involving both element tests and boundary value problems. It has been found that:

- The nonlocal approach is capable of alleviating mesh-dependency intrinsically appearing when softening constitutive models are used within a Finite Element method framework. Indeed, the thickness of the shear band is similar to the characteristic length of the averaging function proposed by Galavi and Schweiger (2010) and is independent of the element size.

- When compared to the reference explicit stress integration scheme, the IMPLEX technique provides extra computability capacities and a reduction of computational cost; an speed-up higher than 4.5 has been obtained.

- Nonlocal integration is also facilitated by the inbuilt mesh adaptivity of PFEM, diminishing the computational cost.

The good performance demonstrated by the numerical simulations reported in this work provides additional confidence to explore further the presented approach for the simulation of more challenging problems; for instance problems involving contact, such as cone penetration or pile installation.

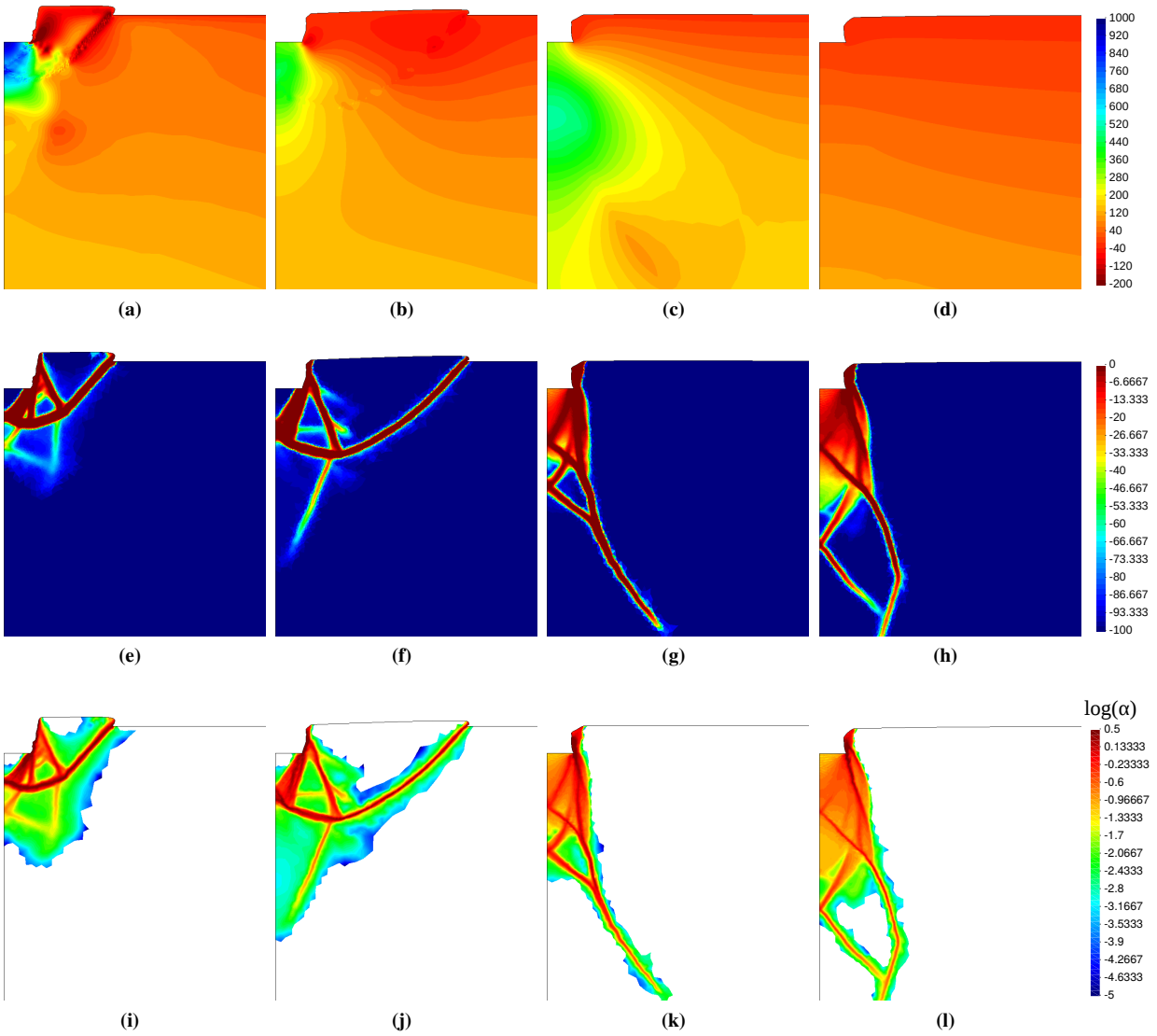

Figure 12: Indentation of rigid, strip footing. Water pressure, plastic variable that accounts for the available bonding resistance, p_t, and accumulated deviatoric plastic strain, α, (in logarithmic scale). From left to right: $k = 10^{-7}$ m/d, $k = 5 \cdot 10^{-4}$ m/d, $k = 5 \cdot 10^{-3}$ m/d and $k = 10^{-1}$ m/d.

Acknowledgements

The financial support of the Ministry of Science and Innovation of Spain through research grant BIA2017-84752-R is gratefully appreciated.

References

Alfano, G. and M. A. Crisfield (2001). Finite element interface models for the delamination analysis of laminated composites: mechanical and computational issues. *International Journal for Numerical Methods in Engineering 50*(7), 1701–1736.

Arroyo, M., R. Castellanza, and R. Nova (2005). Compaction bands and oedometric testing in cemented soils. *Soils and Foundations 45*(2), 181–194.

Arroyo, M., M. Ciantia, R. Castellanza, A. Gens, and R. Nova (2012). Simulation of cement-improved clay structures with a bonded elasto-plastic model: A practical approach. *Computers and Geotechnics 45*, 140 – 150.

Bardet, J. P. and W. Choucair (1991). A linearized integration technique for incremental constitutive equations. *International Journal for Numerical and Analytical Methods in Geomechanics 15*(1), 1–19.

Bathe, K. J. (2006). *Finite element procedures*. Prentice-Hall.

Bažant, Z. P. and M. Jirásek (2002). Nonlocal integral formulations of plasticity and damage: survey of progress. *Journal of Engineering Mechanics 128*(11), 1119–1149.

Bochev, P. B., C. R. Dohrmann, and M. D. Gunzburger (2006). Stabilization of low-order mixed finite elements for the Stokes equations. *SIAM Journal on Numerical Analysis 44*(1), 82–101.

Carbonell, J. M., E. Oñate, and B. Suárez (2013). Modelling of tunnelling processes and rock cutting tool wear with the particle finite element method. *Computational Mechanics 52*(3), 607–629.

Ciantia, M. (2018). A constitutive model for the hydro-chemo-mechanical behaviour of chalk. In *Engineering in Chalk*, pp. 275–281.

Ciantia, M. O., R. Castellanza, and C. Di Prisco (2015). Experimental study on the water-induced weakening of calcarenites. *Rock Mechanics and Rock Engineering 48*(2), 441–461.

Ciantia, M. O., R. Castellanza, and J. A. Fernandez-Merodo (2018). A 3D numerical approach to assess the temporal evolution of settlement damage

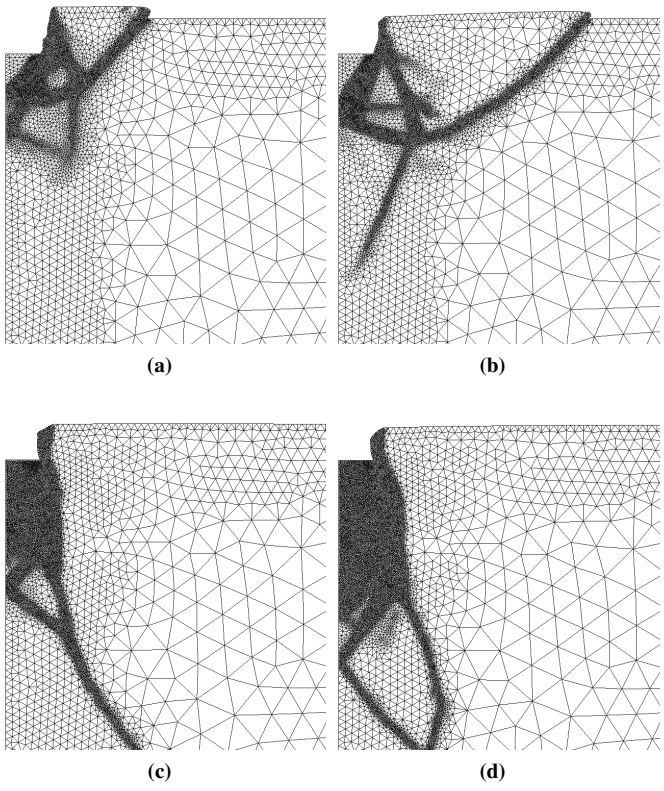

Figure 13: Indentation of rigid, strip footing. Detail of the finite element discretization after a footing indentation equal to $B/2$ for four different permeabilities: $k = 10^{-7}$ m/d, (a), $k = 5 \cdot 10^{-4}$ m/d, (b), $k = 5 \cdot 10^{-3}$ m/d, (c), and $k = 10^{-1}$ m/d, (d).

to buildings on cavities subject to weathering. *Rock Mechanics and Rock Engineering 51*(9), 2839–2862.

Ciantia, M. O. and C. di Prisco (2016). Extension of plasticity theory to debonding, grain dissolution, and chemical damage of calcarenites. *International Journal for Numerical and Analytical Methods in Geomechanics 40*(3), 315–343.

Dadvand, P., R. Rossi, and E. Oñate (2010). An object-oriented environment for developing finite element codes for multi-disciplinary applications. *Archives of Computational Methods in Engineering 17*(3), 253–297.

de Pouplana, I. and E. Oñate (2016). Combination of a non-local damage model for quasi-brittle materials with a mesh-adaptive finite element technique. *Finite Elements in Analysis and Design 112*, 26–39.

Franci, A., E. Oñate, and J. M. Carbonell (2015). On the effect of the bulk tangent matrix in partitioned solution schemes for nearly incompressible fluids. *International Journal for Numerical Methods in Engineering 102*(3-4), 257–277.

Galavi, V. and H. F. Schweiger (2010). Nonlocal multilaminate model for strain softening analysis. *International Journal of Geomechanics 10*(1), 30–44.

Gens, A., M. Arroyo, J. Butlanska, J. M. Carbonell, M. Ciantia, L. Monforte, and C. O'Sullivan (2016). Simulation of cone penetration test: Discrete and continuum approaches. *Australian Geomechanics Journal 51*(4), 169–182.

Gens, A. and R. Nova (1993). Conceptual bases for a constitutive model for bonded soils and weak rocks. In *Geomechanical Engineering of Hard Soils-Soft Rocks*.

Gonzalez, N. A., M. Rouainia, M. Arroyo, and A. Gens (2012). Analysis of tunnel excavation in London Clay incorporating soil structure. *Géotechnique 62*(12), 1095.

Goodarzi, M. and M. Rouainia (2017). Modelling slope failure using a quasi-static MPM with a non-local strain softening approach. *Procedia Engineering 175*, 220 – 225. Proceedings of the 1st International Conference on the Material Point Method (MPM 2017).

Hellweg, H. B. and M. A. Crisfield (1998). A new arc-length method for handling sharp snap-backs. *Computers & Structures 66*(5), 704–709.

Houlsby, G. T. (1985). The use of a variable shear modulus in elastic-plastic models for clays. *Computers and Geotechnics 1*(1), 3–13.

Idelsohn, S. R., E. Oñate, and F. D. Pin (2004). The particle finite element method: a powerful tool to solve incompressible flows with free-surfaces and breaking waves. *International Journal for Numerical Methods in Engineering 61*(7), 964–989.

Jardine, R. J., R. M. Buckley, S. Kontoe, P. Barbosa, and F. C. Schroeder (2018). Behaviour of piles driven in chalk. In *Engineering in Chalk*, pp. 33–51.

Jin, W. and C. Arson (2018a). Anisotropic nonlocal damage model for materials with intrinsic transverse isotropy. *International Journal of Solids and Structures 139-140*, 29 – 42.

Jin, W. and C. Arson (2018b). Nonlocal enrichment of a micromechanical damage model with tensile softening: Advantages and limitations. *Computers and Geotechnics 94*, 196 – 206.

Jirásek, M. and S. Rolshoven (2003). Comparison of integral-type nonlocal plasticity models for strain-softening materials. *International Journal of Engineering Science 41*(13-14), 1553–1602.

Lagioia, R. and R. Nova (1995). An experimental and theoretical study of the behaviour of a calcarenite in triaxial compression. *Géotechnique 45*(4), 633–648.

Larese, A., R. Rossi, E. Oñate, and S. R. Idelsohn (2008). Validation of the particle finite element method (PFEM) for simulation of free surface flows. *Engineering Computations 25*(4), 385–425.

Leroueil, S. and P. R. Vaughan (1990). The general and congruent effects of structure in natural soils and weak rocks. *Géotechnique 40*(3), 467–488.

Liu, M. D. and J. P. Carter (2002). A structured Cam Clay model. *Canadian Geotechnical Journal 39*(6), 1313–1332.

Lloret-Cabot, M., S. W. Sloan, D. Sheng, and A. J. Abbo (2016). Error behaviour in explicit integration algorithms with automatic substepping. *International Journal for Numerical Methods in Engineering 108*(9), 1030–1053.

Lorentz, E. and P. Badel (2004). A new path-following constraint for strain-softening finite element simulations. *International journal for numerical methods in engineering 60*(2), 499–526.

Lu, X., J.-P. Bardet, and M. Huang (2009). Numerical solutions of strain localization with nonlocal softening plasticity. *Computer Methods in Applied Mechanics and Engineering 198*(47), 3702 – 3711.

Mánica, M. A., A. Gens, J. Vaunat, and D. F. Ruiz (2018). Nonlocal plasticity modelling of strain localisation in stiff clays. *Computers and Geotechnics 103*, 138–150.

Monforte, L., M. Arroyo, J. M. Carbonell, and A. Gens (2018). Coupled effective stress analysis of insertion problems in geotechnics with the particle finite element method. *Computers and Geotechnics 101*, 114–129.

Monforte, L., M. Arroyo, A. Gens, and J. M. Carbonell (2015). Explicit finite deformation stress integration of the elasto-plastic constitutive equations. In *Computer Methods and Recent Advances in Geomechanics - Proceedings of the 14th Int. Conference of International Association for Computer Methods and Recent Advances in Geomechanics, IACMAG 2014*, pp. 267–272.

Monforte, L., M. Arroyo, A. Gens, and J. M. Carbonell (2017). Numerical simulation of undrained insertion problems in geotechnical engineering with the Particle Finite Element Method (PFEM). *Computers and Geotechnics 82*, 144 – 156.

Monforte, L., M. Arroyo, A. Gens, and J. M. Carbonell (2018). Hydraulic conductivity from piezocone on-the-fly: a numerical evaluation. *Géotechnique Letters 8*(4), 268–277.

Monforte, L., J. M. Carbonell, M. Arroyo, and A. Gens (2017). Performance of mixed formulations for the particle finite element method in soil mechanics problems. *Computational Particle Mechanics 4*(3), 269–284.

Monforte, L., P. Navas, J. M. Carbonell, M. Arroyo, and A. Gens (2019). Low-order stabilized finite element for the full Biot formulation in soil mechanics at finite strain. *International Journal for Numerical and Analytical Methods in Geomechanics 43*(7), 1488–1515.

Oñate, E., S. R. Idelsohn, M. A. Celigueta, and R. Rossi (2008). Advances in the particle finite element method for the analysis of fluid–multibody interaction and bed erosion in free surface flows. *Computer Methods in Applied Mechanics and Engineering 197*(19-20), 1777–1800.

Oliver, J., A. E. Huespe, and J. C. Cante (2008). An implicit/explicit integration scheme to increase computability of non-linear material and contact/friction problems. *Computer Methods in Applied Mechanics and Engineering 197*(21), 1865–1889.

Oñate, E., S. R. Idelsohn, F. Del Pin, and R. Aubry (2004). The particle finite element method - an overview. *International Journal of Computational Methods 1*(02), 267–307.

Pastor, M., T. Li, X. Liu, and O. C. Zienkiewicz (1999). Stabilized low-order finite elements for failure and localization problems in undrained soils and foundations. *Computer Methods in Applied Mechanics and Engineering 174*(1-2), 219–234.

Pastor, M. and M. Quecedo (1995). A patch test for mesh alignment effects in localized failure. *Communications in Numerical Methods in Engineering 11*(12), 1015–1024.

Potts, D. M. and A. Gens (1985). A critical assessment of methods of correcting for drift from the yield surface in elasto-plastic finite element analysis. *International Journal for Numerical and Analytical Methods in Geomechanics 9*(2), 149–159.

Prazeres, P. G. C., L. A. G. Bitencourt, T. N. Bittencourt, and O. L. Manzoli (2016). A modified implicit–explicit integration scheme: an application to elastoplasticity problems. *Journal of the Brazilian Society of Mechanical Sciences and Engineering 38*(1), 151–161.

Riks, E. (1979). An incremental approach to the solution of snapping and buckling problems. *International journal of solids and structures 15*(7), 529–551.

Rios, S., M. Ciantia, N. Gonzalez, M. Arroyo, and A. Viana da Fonseca (2016). Simplifying calibration of bonded elasto-plastic models. *Computers and Geotechnics 73*, 100 – 108.

Rodríguez, J. M., J. M. Carbonell, J. C. Cante, and J. Oliver (2016). The particle finite element method (PFEM) in thermo-mechanical problems. *International Journal for Numerical Methods in Engineering 107*(9), 733–785.

Rodríguez, J. M., J. M. Carbonell, J. C. Cante, and J. Oliver (2017). Continuous chip formation in metal cutting processes using the particle finite element method (PFEM). *International Journal of Solids and Structures 120*, 81–102.

Rodríguez-Ferran, A. and A. Huerta (2000). Error estimation and adaptivity for nonlocal damage models. *International Journal of Solids and Structures 37*(48-50), 7501–7528.

Rodríguez-Ferran, A., I. Morata, and A. Huerta (2004). Efficient and reliable nonlocal damage models. *Computer methods in applied mechanics and engineering 193*(30-32), 3431–3455.

Rolshoven, S. (2003). *Nonlocal plasticity models for localized failure*. Ph.D. thesis, École Polytechnique Fédérale de Lausanne, Switzerland.

Rouainia, M. and D. Muir Wood (2000). A kinematic hardening constitutive model for natural clays with loss of structure. *Géotechnique 50*(2), 153–164.

Sánchez, P. J., A. Huespe, and J. Oliver (2008). On some topics for the numerical simulation of ductile fracture. *International Journal of Plasticity 24*(6), 1008–1038.

Simo, J. and G. Meschke (1993). A new class of algorithms for classical plasticity extended to finite strains. Application to geomaterials. *Computational Mechanics 11*(4), 253–278.

Simo, J. C. (1998). *Numerical analysis and simulation of plasticity. Handbook of numerical analysis*, Volume 6. Elsevier.

Simo, J. C. and T. J. R. Hughes (1998). *Computational inelasticity*. Springer Science & Business Media.

Sloan, S. W., A. J. Abbo, and D. Sheng (2001). Refined explicit integration of elastoplastic models with automatic error control. *Engineering Computations 18*(1/2), 121–194.

Sołowski, W. T. and S. W. Sloan (2014). Stress integration schemes for unsaturated soils. In *Unsaturated Soils: Research & Applications*, pp. 487–494. CRC Press.

Summersgill, F. C., S. Kontoe, and D. M. Potts (2017a). Critical assessment of nonlocal strain-softening methods in biaxial compression. *International Journal of Geomechanics 17*(7), 04017006.

Summersgill, F. C., S. Kontoe, and D. M. Potts (2017b). On the use of nonlocal regularisation in slope stability problems. *Computers and Geotechnics 82*, 187 – 200.

Taiebat, M., A. M. Kaynia, and Y. F. Dafalias (2010). Application of an anisotropic constitutive model for structured clay to seismic slope stability. *Journal of Geotechnical and Geoenvironmental Engineering 137*(5), 492–504.

Tamagnini, C., R. Castellanza, and R. Nova (2002). A generalized backward Euler algorithm for the numerical integration of an isotropic hardening elastoplastic model for mechanical and chemical degradation of bonded geomaterials. *International Journal for Numerical and Analytical Methods in Geomechanics 26*(10), 963–1004.

Tamagnini, C. and M. Ciantia (2015). A theory of plasticity with generalized hardening for natural geomaterials under mechanical and environmental loading: Constitutive modeling and numerical implementation. In *Computer Methods and Recent Advances in Geomechanics - Proceedings of the 14th Int. Conference of International Association for Computer Methods and Recent Advances in Geomechanics, IACMAG 2014*, pp. 81–90.

Tamagnini, C. and M. O. Ciantia (2016). Plasticity with generalized hardening: constitutive modeling and computational aspects. *Acta Geotechnica 11*(3), 595–623.

Titscher, T., J. Oliver, and J. F. Unger (2019). Implicit-explicit integration of gradient-enhanced damage models. *Journal of Engineering Mechanics 145*(7), 04019040.

Wheeler, S. J., A. Näätänen, M. Karstunen, and M. Lojander (2003). An anisotropic elastoplastic model for soft clays. *Canadian Geotechnical Journal 40*(2), 403–418.

Yapage, N. N. S., D. S. Liyanapathirana, R. B. Kelly, H. G. Poulos, and C. J. Leo (2014). Numerical modeling of an embankment over soft ground improved with deep cement mixed columns: Case history. *Journal of Geotechnical and Geoenvironmental Engineering 140*(11), 04014062.

Zhang, X., K. Krabbenhoft, and D. Sheng (2014). Particle finite element analysis of the granular column collapse problem. *Granular Matter 16*(4), 609–619.

Zienkiewicz, O. C., M. Huang, and M. Pastor (1995). Localization problems in plasticity using finite elements with adaptive remeshing. *International Journal for Numerical and Analytical Methods in Geomechanics 19*(2), 127–148.